On-Chip Laser-Power Delivery System for Dielectric Laser Accelerators

Tyler W. Hughes,* Si Tan,† Zhexin Zhao, Neil V. Sapra, Kenneth J. Leedle, Huiyang Deng, Yu Miao, Dylan S. Black, Olav Solgaard, James S. Harris, Jelena Vuckovic, Robert L. Byer, and Shanhui Fan
Stanford University, Stanford, California 94305, USA

R. Joel England
SLAC National Accelerator Laboratory, Menlo Park, California 94025, USA

Yun Jo Lee and Minghao Qi
Purdue University, West Lafayette, Indiana 47907, USA

(Received 18 September 2017; revised manuscript received 16 February 2018; published 14 May 2018)

We propose an on-chip optical-power delivery system for dielectric laser accelerators based on a fractal "tree-network" dielectric waveguide geometry. This system replaces experimentally demanding free-space manipulations of the driving laser beam with chip-integrated techniques based on precise nanofabrication, enabling access to orders-of-magnitude increases in the interaction length and total energy gain for these miniature accelerators. Based on computational modeling, in the relativistic regime, our laser delivery system is estimated to provide 21 keV of energy gain over an acceleration length of 192 μm with a single laser input, corresponding to a 108-MV/m acceleration gradient. The system may achieve 1 MeV of energy gain over a distance of less than 1 cm by sequentially illuminating 49 identical structures. These findings are verified by detailed numerical simulation and modeling of the subcomponents, and we provide a discussion of the main constraints, challenges, and relevant parameters with regard to on-chip laser coupling for dielectric laser accelerators.

DOI: 10.1103/PhysRevApplied.9.054017

I. INTRODUCTION

In recent years, dielectric laser accelerators (DLAs) have demonstrated acceleration gradients (energy gain per unit length) approaching 1 GV/m [1–9], several orders of magnitude higher than those attainable by conventional linear accelerator systems based on microwave-driven metallic waveguide structures [10]. This breakthrough is made possible by the advent of advanced nanofabrication techniques [11–15] combined with the fact that dielectric materials may sustain electric fields close to 10 GV/m when illuminated by ultrafast near-infrared laser pulses [16–18]. High acceleration gradients may allow DLAs to accomplish significant energy gains in very short lengths, which would enable numerous opportunities in fields where compact and low-cost accelerators would be useful, such as medical imaging, radiation therapy, and industrial applications [19–21].

Since DLA structures are already driven at their damage thresholds, apart from finding methods to increase material damage thresholds, achieving high total energy gain from a DLA fundamentally requires extending the interaction length between the incoming laser pulse and the particle beam. This interaction length is limited not only by the longitudinal and transverse stability of the electron beam [22,23] but also by the laser delivery system, which is the focus of this work. Several proof-of-principle DLA experiments [1,24] have demonstrated high acceleration gradients using free-space manipulation of the laser pulse, including lensing, pulse-front tilting [25–27], and multiple driving lasers [28,29]. However, these techniques require extensive experimental effort to perform and the system is exceedingly sensitive to angular alignment, thermal fluctuations, and mechanical noise. By replacing free-space manipulation with precise nanofabrication techniques, an on-chip laser-power delivery system would allow for orders-of-magnitude increases in the achievable interaction lengths and energy gains from a DLA.

In designing any laser-power delivery system for a DLA, there are a few major requirements to consider. (1) The optical-power spatial profile must have good overlap with the electron-beam side profile. (2) The laser pulses must be appropriately delayed along the length of the accelerator to arrive at the same time as the moving electron bunches. (3) The optical fields along each section of the accelerator must, ideally, be of the correct phase to avoid dephasing between the electrons and the incoming

*twhughes@stanford.edu
†stan1987@stanford.edu

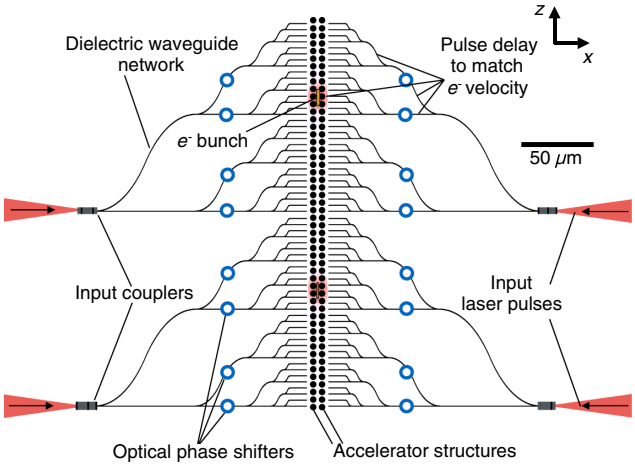

FIG. 1. Two stages of the DLA laser coupling tree-network structure. The electron beam travels along the z axis through the center of this structure. The laser pulses are side coupled with optical power, shown in red. Black regions define the on-chip waveguide network. Blue circles represent the optical phase shifters used to tune the phase of the laser pulse. This geometry serves to reproduce the pulse-front-tilt laser delivery system outlined in Ref. [27] in an integrated optics platform (Supplemental Material Ref. [30]).

laser fields. To accomplish all three of these requirements, we introduce a method for on-chip power delivery which is based on the fractal "tree-network" geometry introduced in Fig. 1. In this paper, we provide a systematic study of the structure's operating principles, the optimal range of the operating parameters, and the fundamental trade-offs that must be considered for any on-chip laser coupling strategy of the same class. Through detailed numerical modeling of this design, we estimate that the proposed structure may achieve 1 MeV of energy gain over a distance less than 1 cm by sequentially illuminating 49 identical structures.

The paper is organized as follows: In Sec. II, we introduce the working principles and components of the proposed laser coupling system. In Sec. III, we make an overview of the main constraints facing this system. In Sec. IV, we present the findings of a parameter study investigating the structure. In Sec. V, we discuss the limitations and benefits of the proposed structure. In Sec. VI, we propose future directions for this work before concluding in Sec. VII. The assumptions and values used in the parameter study are validated by discussion in the appendixes.

II. SYSTEM MODEL

We first introduce the proposed tree-network waveguide geometry, which is diagramed in Fig. 1. The electron beam to be accelerated is propagating along the z axis in the central accelerator gap. We first couple the laser pulses to the on-chip dielectric waveguides by use of input couplers. The optical power is then split a series of times and directed by waveguide bends to illuminate the entire length of the accelerator gap. Integrated phase shifters are used to tune the phase of each pulse upon exiting the waveguides and may be optimized for maximum acceleration. The accelerating structures are placed adjacent to the waveguide outputs. In this work, we choose to investigate silicon dual-pillar accelerator structures similar to those used in Ref. [3]. The entire device is mirrored over the center plane and is driven by laser inputs on each side. Two stages of the structure are shown in Fig. 1, although several more may be implemented in series, assuming the availability of several phase-locked laser sources. Electron-beam focusing elements may be implemented between stages as needed. For more information, a detailed overview of the individual components, such as input couplers, waveguide bends, phase shifters, and DLA structures is given in Appendix A.

A fractal waveguide geometry is chosen as it evenly illuminates the accelerator gap with minimal use of 50:50 beam splitters. Furthermore, the waveguide bends are designed such that the laser pulse arrival at the accelerator gap is delayed to coincide with the arrival of the electron bunch as it propagates through the structure. This requirement sets strict conditions on the bending radius required at each section, which is derived in Appendix B.

III. CONSTRAINTS

In the analysis of our system, we consider four main factors that will ultimately limit the acceleration gradients and make energy gains attainable.

(a) Laser-induced damage of the DLA and waveguide materials. To avoid damage of the structure, the electric fields in the system may never exceed the damage thresholds of the dielectrics used. The laser damage threshold for dielectric materials is highly favorable at short pulse durations, with sustainable peak powers that scale roughly as $\tau^{-1/2}$ for $\tau > 1$ ps and approach τ^{-1} scaling for femtosecond pulses [16,31]. Amongst the materials considered in this work, SiO_2 has the highest damage fluence threshold, 2.5 J/cm^2, at a 800-nm wavelength, followed by Si_3N_4, at 0.65 J/cm^2, and Si, at 0.18 J/cm^2 [32]. For a 100-fs pulse propagating in vacuum, these damage fluence numbers correspond to peak fields of 13.7, 7.0, and 3.7 GV/m, respectively.

(b) Optical nonlinearities in the materials. Optical nonlinear effects are encountered when the optical pulse propagates through the waveguides and may cause significant pulse distortion, resulting in either damage or a dramatic reduction of the acceleration gradient. Through a full treatment given in Appendix C, we find that the most prominent nonlinear effect in our structure is self-phase modulation (SPM). For a pulse with a given peak power, the effects of SPM scale in proportion to the lengths of the waveguide sections.

(c) Power loss. The tree-network structure introduces several sources of power loss: (1) input coupling loss, (2) splitting loss, (3) bending loss, and (4) waveguide scattering loss. Waveguide power loss due to scattering must be considered for structures with stage lengths greater than the centimeter scale [33]. However, we neglect these effects in this work because we focus on millimeter or shorter waveguide segments.

(d) DLA structure resonance characteristics versus input pulse bandwidth. The DLA structures are designed to resonantly enhance the optical fields. The field enhancement is proportional to the square root of the quality factor of the DLA structures (similar to an optical cavity), which can be approximated by a Lorentzian spectrum. This resonance is used to increase the acceleration gradient while avoiding damage at the input facet. However, if the pulse bandwidth is large with respect to the bandwidth of the accelerator, the pulse does not efficiently couple to the DLA structure.

IV. PARAMETER STUDY

With the system components and constraints introduced, we now present a parameter study to understand the fundamental trade-offs and optimal working parameters of an on-chip optical-power delivery system for a DLA of this class. A software package [34] was written to separately simulate each component and combine the results to generate an estimate for the acceleration gradient and energy gain assuming a set of parameters which are outlined in Table I. The values of these parameters are validated in Appendix A, where we go into detail about the individual components of this design.

For a given pulse duration (τ) and DLA quality factor (Q), the minimum peak electric field of the input pulse (E_0) required to encounter each damage or nonlinearity constraint is modeled using approximations, which are derived fully in Appendix D and summarized below:

TABLE I. Parameters assumed in the paper.

Parameter	Symbol	Value	Units
Wavelength	λ	2	μm
Electron speed/speed of light	β	1	⋯
DLA periods per waveguide	M	3	⋯
Input-coupler efficiency	η_c	0.6	⋯
Splitting efficiency	η_s	0.95	⋯
Bending efficiency	η_b	0.95	⋯
Accelerating gradient at $Q = 1$	$G_{Q=1}$	0.0357	E_0
Input coupler—First split length	L_0	10	μm
DLA pillar radius	R_{pillar}	981	nm
DLA acceleration gap	d	400	nm
Material or gap field enhancement factor	f_m	2	⋯

(1) The input electric-field amplitude must be smaller than the damage threshold $E_d(\tau)$ of the input-coupler material,

$$E_0 < E_d(\tau). \tag{1}$$

(2) The input electric-field amplitude must be small enough to not damage the accelerator structure, with damage threshold $E_d(\tau)$,

$$E_0 < E_d(\tau)\frac{2^{N_s/2}}{f_m\sqrt{Q}}(\eta_c\eta_s^{N_s}\eta_b^{N_s})^{-1/2}. \tag{2}$$

(3) The input electric-field amplitude must be small enough to avoid SPM effects in the waveguides,

$$E_0 < \left(\frac{2\lambda}{n_2^{(\text{eff})}nc_0\epsilon_0\eta_c}\sum_{i=0}^{N_s}\frac{2^i}{\eta_s^i\eta_b^iL_i}\right)^{1/2}. \tag{3}$$

Here, f_m is the field enhancement factor in the DLA structure, Q is the DLA quality factor, $n_2^{(\text{eff})}$ is an effective nonlinear refractive index that takes into account the proportions of each material in the waveguide geometry, as defined in Appendix D, L_i values are the waveguide segment lengths for the longest path from input coupler to accelerator, and n is the refractive index of the waveguide core. We model the input coupling simply by multiplying the optical power by the input-coupler efficiency. After the pulse is coupled and encounters losses from splitting and losses at each section, the peak electric field that reaches the accelerator structure (E_{out}) is given by

$$E_{\text{out}} = E_0(2^{-N_s}\eta_c\eta_s^{N_s}\eta_b^{N_s})^{1/2}. \tag{4}$$

We note that the presence of power splits concentrates the optical power at the input facet of the structure relative to the output facet.

To model the DLA structures and estimate the acceleration gradient achievable in this geometry, we use a two-dimensional finite-difference frequency-domain (FDFD) method [35] to simulate a waveguide feeding Si dual-pillar structures. The pillars are assumed to have infinite extent out of the plane, neglecting fringing effects. The phase at each output waveguide is assumed to be at its optimal value for maximum acceleration through the entire section. To compute the acceleration gradient, we must do the following: (1) Use the FDFD method to compute the acceleration gradient over a discrete range of frequencies. (2) Fit a Lorentzian to the frequency response of the DLA structure, following the discussion in Appendix E. (3) Using the parameters extracted from this fit, scale the response to the Q factor of interest. (4) Use the input pulse spectrum and fit parameters to compute the acceleration gradient, following the derivation in Appendix F.

We first examine a single "stage" with a length of 192 μm. In this work, we define a stage as an accelerator section with

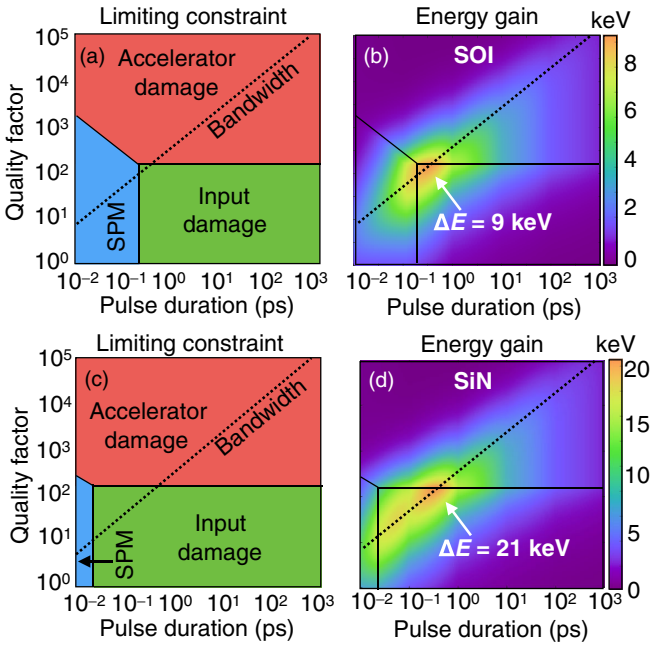

FIG. 2. Results from the parameter study. A single stage of the tree-network structure is simulated, with a stage length of 192 μm, corresponding to five power splits and $2^5 = 32$ output ports. In (a) and (b), silicon-on-insulator (SOI) waveguides are assumed. In (c) and (d), Si_3N_4/SiO_2 waveguides are assumed. For each Q factor and pulse duration, we compute the maximum input field achievable before damage or nonlinearity occurs. The different-colored regimes in (a) and (c) correspond to different limiting constraints, as labeled in the plots. The dotted line corresponds to the minimum pulse duration before the pulse bandwidth exceeds the DLA resonator bandwidth. The energy gain from one section is plotted in (b) and (d).

a single input laser. This number is chosen as it gives a reasonable balance between acceleration gradient and energy gain. Over a range of pulse durations (τ) and Q factors (Q), we first compute the minimum peak electric field at input that will cause either damage or nonlinear pulse distortion using Eqs. (1)–(4). Then, for relativistic electrons, we use the assumed parameters to compute the achievable acceleration gradient and energy gain. In Fig. 2, we show the limiting constraints for each τ and Q, as well as the energy gain from a single stage. This information is presented separately for waveguide core materials of Si and Si_3N_4.

From Fig. 2, we see that, for a given geometry, there is an optimal combination of τ and Q where the energy gains and acceleration gradients are maximized. For a structure with a stage length of 192 μm, this point is at $\tau = 341/322$ fs and $Q = 157/154$ for waveguide cores made of Si/Si_3N_4. A full list of the results are displayed in Table II. Using a SiN waveguide system, we may expect to achieve 1 MeV of energy gain at 108 MV/m gradients by running 49 stages in series. However, these are conservative values based upon a few well-established waveguide approaches and materials, and they therefore represent a lower bound on the achievable gradient.

TABLE II. Optimal results from the parameter study, for waveguides with material platforms of SOI and SiN.

Metric	Value (SOI)	Value (SiN)	Units
Acceleration gradient	45.3	107.5	MV/m
Energy gain per stage	8.7	20.6	keV
Input peak electric field	1.0	2.4	GV/m
Pulse duration	341	322	fs
DLA Q factor	156.7	154.0	···
Pulse energy at input coupler	0.36	11.3	nJ
Number of stages for 1 MeV	116	49	···
Stage length	192	192	μm
Waveguide core width	0.78	2	μm
Waveguide core height	220	400	nm

V. DISCUSSION

There are several competing effects that lead to the existence of this optimal point. First, for a given pulse peak power, shorter pulse durations generally lead to higher acceleration gradients because the materials exhibit higher electric-field damage thresholds. However, this effect is limited by the occurrence of SPM at a certain input field. Furthermore, if the pulse is too short with respect to the Q factor of the DLA structures, the pulse does not couple efficiently to the accelerator gap due to the pulse bandwidth being larger than the structural bandwidth. Second, higher Q factors lead to resonantly enhanced fields inside of the DLA structure and higher acceleration gradients as a result [36]. However, if the Q factor is too high, these enhanced fields cause the accelerator structures to damage.

To investigate how these results depend on the stage length, we run several of these simulations over a range of structures with different numbers of splits, keeping track of the optimal τ, Q, acceleration gradient, and energy gain of each structure. The results are presented in Fig. 3.

From Fig. 3(a), we note that, as the stage lengths become longer, the achievable acceleration gradients decrease due to the increased losses introduced by the greater number of splits, combined with the increased nonlinearities and concentration of optical power at the input facet. On the other hand, the energy gain increases with greater stage length. Thus, there is an intrinsic trade-off between having a high acceleration gradient and a large energy gain per laser input, suggesting that the choice of stage length should be determined by the acceleration gradients and energy gains required by the application. For instances where a high acceleration gradient is preferred, a smaller stage length per laser is optimal, meaning fewer splits. However, for applications where high total energy gain is a more important figure of merit, it may be beneficial to use a coupling structure with many splits and long stage length, but a lower acceleration gradient. These metrics will also depend on the availability of several phase-locked laser sources and the experimental difficulties associated with coupling them to several input couplers. Because of the

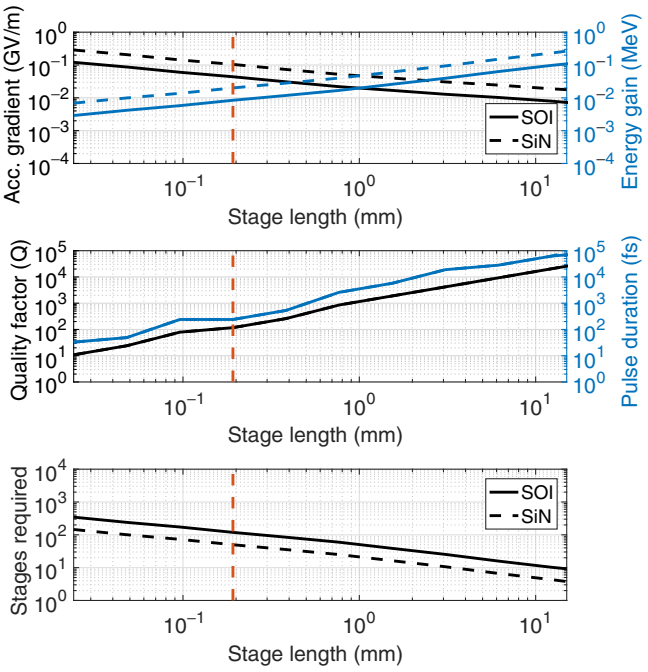

FIG. 3. Scaling of optimal parameters as a function of the stage length. The red dotted line corresponds to a stage length of 192 μm, which is the length used in Fig. 2. (a) The optimal energy gains and acceleration gradients as a function of stage length for both SOI and SiN structures. (b) The optimal set of pulse duration and the Q factor corresponding to the highest energy gain and acceleration gradient at each stage length. The curves for the SOI and SiN materials are overlaid. (c) The number of stages required to reach 1 MeV of total energy gain as a function of individual stage length.

challenges introduced by concentrating the optical power at a single input facet, there would be a significant improvement on these results by considering input schemes that may couple a single beam directly to several waveguides. While this is outside of the scope of this paper, it is a promising avenue to explore for these systems.

From inspecting Fig. 3(b), we see that the optimal τ and Q increases as the structure becomes larger. Thus, the longer the stage length we wish to supply with this tree-network geometry, the more resonance we require in the DLA structures. For a longer stage length, more splits must be performed, which puts an additional burden on the input facet relative to the DLA structure. This fact, in turn, requires greater resonant enhancement at the accelerator gap to offset, and a subsequently larger τ to match the structural bandwidth.

VI. OUTLOOK

We now discuss the outlook of the results of this parameter study and present some methods for improving on the findings. First, we notice that SiN waveguide systems may supply much higher acceleration gradients than SOI systems. This observation is due to the favorable

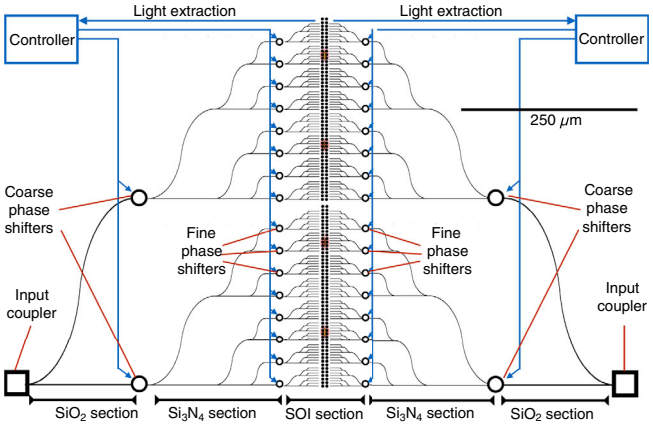

FIG. 4. Schematic of a hybrid structure for DLA laser coupling. (Center) A SOI tree-network–DLA geometry optimized for tight bends and compact waveguides. This section is fed by a Si_3N_4/SiO_2 waveguide section with a relatively higher damage threshold, and lower nonlinearities. This section is then fed by an all-SiO_2 power delivery section, as described in the discussion section. Coarse and fine phase shifters are used in different splitting sections.

damage and nonlinear properties of Si_3N_4 compared to Si. However, as we show in Appendix A, SiN waveguides have high bending loss at bend radii below 50 μm due to the low refractive index of Si_3N_4 compared to Si. Therefore, to mitigate the effects of damage and nonlinearities in our waveguide system while maintaining the bending radii required for pulse delay, one solution is to implement a hybrid system comprising a laser-power delivery system optimized for high power handling to feed a series of smaller tree-network structures optimized for tight bends. A diagram of this setup is given in Fig. 4.

Waveguiding systems for this high-power-handling region may be based on hollow-core photonic crystals, high-damage-threshold materials, such as silica or silicon nitride, or weakly guided waveguide modes. The section closer to the DLA can then be implemented in silicon-on-insulator (SOI) structures, allowing for tight bending radii, compact waveguide networks, and fine phase control. The DLA structures may also be integrated directly on the same chip as the inner power delivery system. Multiple of these hybrid systems may be driven in series, each with an individual driving laser. The relative merits of large-stage-length power delivery systems vs multiple driving lasers depends on their respective engineering challenges, such as chip-to-chip coupling [37,38], the alignment and stability of input coupling multiple lasers, and the availability of these sources.

Furthermore, based on the presented geometry, there is a clear need for resonant DLA structures to enhance the fields at the accelerator gap. For the parameters discussed, the optimal Q factors are shown to be around 150. Previous work on optimizing DLA structures for a high acceleration gradient has shown that periodic dielectric mirrors may be

useful in raising quality factors and field enhancement in DLA structures [39–42]. However, achieving DLA structures with these Q factors may be difficult with current fabrication tolerances. Furthermore, even slight deformation due to both electron collision with the DLA structure and the presence of high-power optical pulses would degrade the Q factors of fabricated structures. Therefore, experimental verification is required to determine whether such resonant structures can survive operation in a DLA.

One final set of attractive options for further improving the acceleration gradients and energy gains achievable with an on-chip waveguide power delivery system involve engineering the group-velocity dispersion (GVD) of the waveguides. One strategy involves prechirping the input pulse to compensate for the GVD. Then, the optical power may be initially spread in the temporal domain, mitigating damage bottlenecks near the input facet. Later, with the presence of the GVD, the structure may be designed such that the pulse recompresses at the accelerator structure. Additionally, we may use the GVD to balance out SPM effects in our waveguides. With the proper amount of GVD, a temporal soliton may be formed for a given power, which propagates without distortion, potentially allowing for higher operating powers and acceleration gradients. A similar technique was recently demonstrated to compensate for the SPM effects in short DLA structures [7].

These are promising avenues for exploration, but they are not considered in this work with the intention of establishing a conservative baseline for the merits of on-chip laser coupling. The next stage of this work will involve experimentally verifying the parameters assumed, including the waveguide damage thresholds, input coupling loss, splitting loss, bending loss, and acceleration gradients. An additional exploration of other material systems, such as Ta_2O_5 [43] and Ga_2O_3, may offer waveguides and components with loss, nonlinearity, and damage-threshold characteristics superior to the material systems assumed in this work. With these issues investigated, a proof-of-principle optical test will be performed on a simple system before acceleration experiments with electron beams are performed.

VII. CONCLUSION

In this paper, we present a method for accomplishing chip-based, optical laser-power delivery for DLA applications along with a systematic study investigating the damage and nonlinearity constraints and the trade-off between pulse characteristics and DLA resonance. For a stage length of 192 μm, our method predicts acceleration gradients greater than 100 MV/m, and 1 MeV of energy gain in less than 1 cm with 49 structures integrated in series.

We conclude that an on-chip laser coupling system is a promising avenue of exploration for DLA technology. Using the known parameters of existing waveguide technology, we may couple laser sources to an accelerator on a chip with a reasonable acceleration gradient. Additionally, our proposal has a major advantage over free-space laser coupling techniques in that it provides an on-chip solution for scalable stage length, which enables access to longer interaction lengths, better integration with DLA structures, and greater total energy gains. These findings are a crucial and necessary step towards bringing DLA from the proof-of-principle to the application stage.

ACKNOWLEDGMENTS

We wish to acknowledge everyone in the ACHIP Collaboration for their guidance and comments, with special thanks to Kent Wootton. This work was supported by the Gordon and Betty Moore Foundation (Grant No. GBMF4744).

APPENDIX A: STRUCTURE COMPONENTS

To validate the assumptions made in the parameter study, we now discuss the individual components involved in the on-chip laser coupling system.

1. Input coupling

The proposed structure first requires a strategy to couple light from the pump laser to the on-chip optical waveguides. We focus on free-space coupling to the input facet via a surface grating, eliminating the need for single-mode-fiber delivery. Our laser and macroscopic optical components are capable of handling pulse energies far beyond that which would cause damage to the structure. Bare single-mode fibers also have damage thresholds high enough to withstand these laser pulses, but the large amount of dispersion introduced (associated with the relatively long length of >1 mm) makes them unsuitable for delivery to the chip.

In general, couplers must have (1) high coupling efficiency, (2) a bandwidth large enough to couple to the entire pulse spectrum, and (3) high power handling and minimized hot spots. Input coupling may be accomplished by the use of end coupling, focusing the laser beam directly onto the waveguide cross section, or vertical coupling schemes, such as grating couplers. In SOI systems, end coupling can achieve insertion losses as low as 0.66 dB (85.9%) over a bandwidth of roughly 10 THz [44], but it is cumbersome to perform experimentally for a large number of inputs and constrains the input and output coupling ports to be located on the edges of the chip. Vertical couplers provide the benefit of relative flexibility in alignment and positioning on chip. The coupling efficiency of these devices varies drastically depending on the complexity of the grating-coupler design, from an efficiency of $>30\%$ to $>90\%$ [45]. However, highly efficient broadband couplers capable of sustaining large bandwidths still provide design challenges, with the state-of-the-art fully etched structures able to provide 67% coupling efficiency with a 3-dB bandwidth of 60 nm at 1550 nm [46]. In this paper, we assume a coupling power efficiency of 60% with a

substantially wide bandwidth to accommodate that of our pulse (up to about 117 nm for a 50-fs pulse), which is reasonably achievable with end coupling. Additional investigation into the design of ultrabroadband vertical couplers must be considered to guarantee coupling of the femtosecond pulsed lasers.

2. Waveguides

Waveguides are a critical component of laser coupling. Schematics of the waveguide cross sections and their field distributions are shown in Fig. 5. We explore two general classes of waveguiding systems: (1) tightly confined systems and (2) weakly confined systems. Weakly confined waveguide modes have a small difference between mode effective index and cladding index, which results in the optical power being spread over a larger area and into the cladding material, which generally has preferable damage and nonlinearity properties. However, as we discuss in the next section, our simulations show that weakly confined modes, with $n_{\mathrm{eff}} - n_{\mathrm{core}}$ values of about 0.1, have almost 0% power transmission for bend radii less than 10 μm. In our tree-network structure, we require bend radii of this order to achieve the required pulse delay to matching to the electron bunch; therefore, weakly guided waveguides are not considered for the particular tree-network structure in this parameter study.

We explore material systems of SOI and Si_3N_4/SiO_2 structures due to their common use as waveguide core materials. SOI-based waveguides would be simpler to integrate with the silicon DLA structure and electron gun and there exists a much larger body of previous work on fabrication of silicon material systems for applications such as phase control, especially in the LIDAR community [48,49]. However, Si_3N_4/SiO_2 waveguides have favorable nonlinear and damage properties compared to those made from SOI. As mentioned, there are several other material systems that could also be explored for low loss, low nonlinearity, and high damage thresholds. Ta_2O_5 [43] and Ga_2O_3 are promising candidates that will be investigated in future studies.

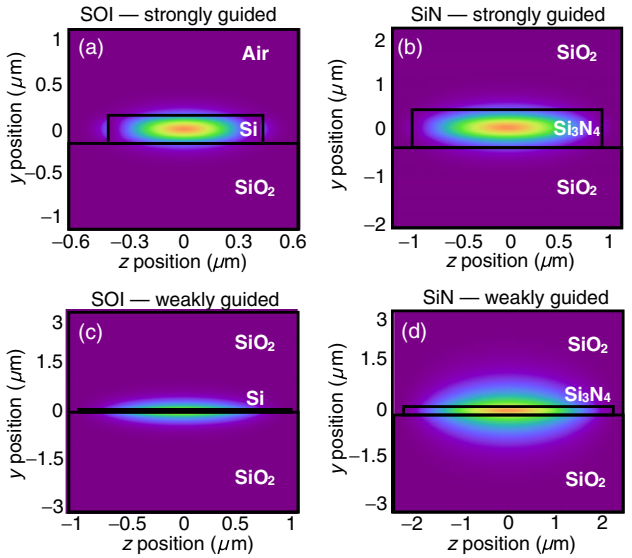

FIG. 5. Waveguide geometries and corresponding horizontal electric-field components [47]. (a),(b) Strongly confined modes. (c),(d) Weakly confined modes. (a) and (c) are SOI material platforms, whereas (b) and (d) are Si_3N_4/SiO_2 materials. Waveguide core heights in (a)–(d) are given by 220, 400, 60, and 100 nm, respectively. Waveguide core widths are given by 0.78, 1.6, 2, and 4 μm, respectively.

3. Splitters

After the initial input coupling step, splitters are used to distribute the laser power along the DLA structure. Splitters further contribute to insertion loss. An experimental characterization of Y splitters indicates losses on the order of 1 dB [50]. However, recent advances in topology optimization techniques have allowed for alternative designs with much higher efficiencies. Using "particle swarm optimization" [51], devices have been produced with theoretical insertion losses of 0.13 dB and an experimentally determined value of 0.28 ± 0.02 dB [50]. As even more sophisticated techniques of optimization have been developed, the insertion loss of simulated designs has reached 0.07 dB [52]. Adjoint-based optimization methods have been further expanded to enforce fabrication constraints on the permitted designs, thus allowing one to expect greater agreement between simulated and fabricated structures [53]. As a consequence of the rapid progress made in this field and the efforts to ensure robustness of the device to fabrication tolerance, we use an insertion loss per splitter of 0.22 dB, or 95% efficiency, for the parameter study.

4. Bends

The bending radius is uniquely chosen to give enough extra propagation distance to provide a delay of the pulse between different output ports, which is matched to the electron velocity. We derive conditions on the radius of curvature required for each bend for the particular tree-network structure in Appendix B. The required radius depends on the electron velocity (βc_0) and group index of the waveguide mode (n_g), and it becomes smaller as the waveguides approach the DLA structure. Assuming the tree-network geometry used in this work, there is a condition on the group index of the waveguide system that may achieve the required delay given an electron speed,

$$n_g \beta \geq 1. \tag{A1}$$

Thus, for subrelativistic electrons ($\beta < 1$), higher-index materials are required for the waveguides. For example, for a β value of 1/3, a group index of $n_g > 3$ is required, which may not be satisfied by a standard SiN waveguide geometry. Thus, in subrelativistic regimes, SOI waveguides are the optimal choice.

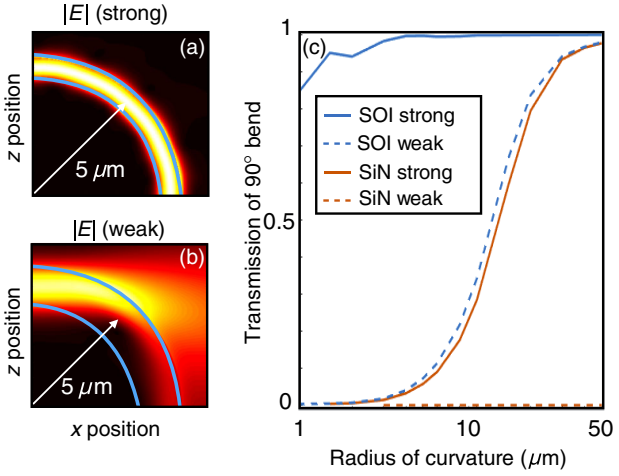

FIG. 6. (a) Electric-field amplitude for a strongly guiding SOI waveguide. (b) Electric-field amplitude for a weakly guiding SOI waveguide. (c) Comparison of bending loss as a function of bend radius for the four waveguides from Fig. 5.

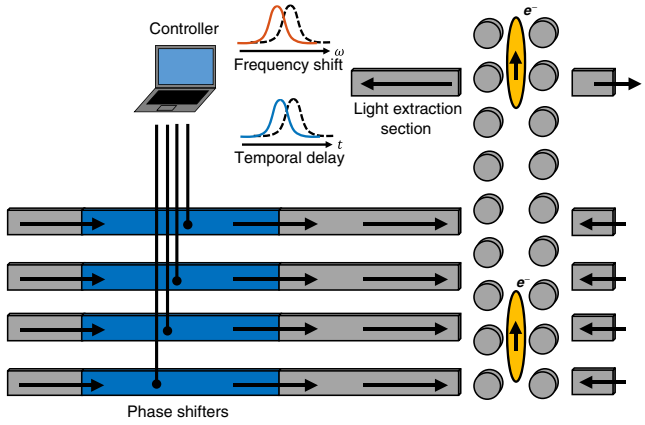

FIG. 7. Idealized schematic of a feedback system for automatic phase control. A dedicated light extraction section is added to the accelerator. Light is radiated from the electron beam that is transverse to the DLA structures, and the frequency content and/or timing of the light is sent to a controller. The phase shifts of each waveguide are optimized with respect to either the frequency or the delay of the signal.

Figure 6 shows the optical-power transmission through a series of bends and waveguide geometries using the FDFD method [35] and an established two-dimensional approximation to the three-dimensional structure [54]. For tightly confined SOI waveguide modes, the bending radius can reach as low as 2 μm before there is significant loss. However, for weakly confined SOI modes and strongly confined SiN modes, the power transmission is less than 50% until the radius exceeds 20 μm. For our purposes, this kind of bending loss is unacceptable, as radii on the order of 10 μm are required close to the DLA structure to perfectly match the electron velocity. However, if we relax the delay requirement in favor of larger bend radii, we may still use strongly confined SiN modes. Based on a calculation following Appendix B, if we wish to keep all SiN waveguides above a 40-μm radius of curvature, we will experience a 25-fs mismatch in peak pulse arrival to electron arrival. For a pulse duration of 250 fs, this mismatch has a negligible effect on the acceleration gradient. Therefore, in our parameter study, we assume strongly confined waveguide modes and bends that are large enough to achieve a transmission of 95%. Many of these issues may be reconciled by choosing a hybrid waveguide system, as shown in Fig. 4, in which different materials and waveguide modes are used at different distances from the central DLA structure. We do not consider these options directly in our parameter study.

5. Phase shifters

Phase shifters are an essential component in the DLA system for ensuring proper phase matching between the electrons and photons. While it is simple to do phase tuning in free space for a single-stage DLA with macroscopic delay stages, waveguide-integrated phase shifters for long interaction or multistage DLAs will be experimentally complicated. To achieve a sizable energy gain and gradient over a given interaction length, high levels of precision and stability in the phase of each section are required.

To illuminate the importance of precision phase shifters, a Monte Carlo simulation is performed in which the output phase of each waveguide is perturbed from its optimal value by a random amount. This work finds that, for a stage length of 1 mm, phase stability and precision of greater than $1/100$ of a radian (0.16% of a cycle) is required to achieve a sustained energy gain within 90% of the maximum achievable amount.

There are a few strategies to implement integrated phase shifters, including the use of (1) the thermal or thermal-optic effect [49,55], (2) the electro-optic effect, and (3) mechanical techniques, such as piezoelectric controlled elements [56]. For this application, we require a full 2π range of phase control of each output port with a resolution of $1/100$ of a radian, and a modulation bandwidth of approximately 1 kHz to correct for environmental perturbations.

Rather than supplying each waveguide output port with a phase shifter with these properties, it may be possible to have dedicated "fine" and "coarse" phase shifters as we move through the splitting structure. Furthermore, some degree of a relatively fixed phase between output ports may be accomplished by precision fabrication.

To further mitigate the challenges associated with operating these multiple phase shifters during acceleration, we may implement a feedback control loop, which is described in Fig. 7. In this setup, the quantity of interest, such as electron energy gain, can be measured at the end of a section and optimized with respect to the individual phase shifters in the power delivery system without explicit knowledge of the electron-beam dynamics.

6. DLA structures

We assume silicon dual-pillar DLA structures in the parameter study, but the choice is arbitrary and can be changed to other materials or designs depending on the fabrication constraints. In Fig. 8, we show an example of the setup considered in the parameter study, simulated with the FDFD method. The pillar radius is 981 nm and the gap width is 400 nm. Three periods of DLA are powered by a single waveguide and periodic boundary conditions are used in the z direction. Wakefields and transverse deflections are ignored for simplicity, as these simulations are intended to provide an estimate of the resonant enhancement, acceleration gradient, and accelerator damage threshold. The waveguide refractive index is approximated using Ref. [54]. To model the frequency response of our structure, following the discussion in Appendix E, a frequency scan is performed and fit to a Lorentzian.

Resonant enhancement in the dual pillars is clearly visible and can be accomplished by optimizing the spacing and radius parameters. It is also clear that the two surrounding DLA cells are slightly out of phase with the center cell. This effect is caused by the lack of translational symmetry in the input optical beam in the z direction and will lower the acceleration gradient. From our Lorentzian fit, a Q value of 152 ± 29 is determined.

Coupling efficiently from waveguides to DLA structures may be done by optimizing the structure parameters. For an optimized structure, back reflection may be minimized. It will be of great importance in future experiments to integrate the waveguide system and the DLA structure on the same chip. Thus, the height of the pillar structure may be constrained to be equal to that of the waveguide core, and 500-nm-thick SOI platforms may be a good starting point for testing these integrated systems.

One waveguide is able to serve multiple DLA periods. However, simulations suggest that additional periods of the DLA per waveguide do not significantly increase the total energy gain achievable from a single waveguide. Thus, the spacing between waveguides must be large enough to eliminate cross talk, but small enough to ensure high acceleration gradients.

7. Beam loading and longitudinal wakes

The fundamental unit cell of the proposed accelerator design, depicted in Fig. 8, consists of a structure segment of three periods $\Delta z = 3\lambda$ fed by a single laser pulse of the multibranch network with the duration $\tau = 250$ fs. It is shown in Ref. [6] that the coupling efficiency of the laser field to a point charge q for the side-coupled geometry used here is analogous to Eq. (7) of Ref. [57], which considers a traveling-wave mode in a cylindrical structure with group velocity $\beta_g c$, under the substitution $\beta_g/(1-\beta_g) \to \Delta z/\tau c$, which gives a coupling efficiency $\eta_q = qG\Delta z/P\tau$. Here, P is the laser mode power and $G = G_0 - G_H$ is the loaded gradient, where G_0 is the unloaded value and G_H is a retarding field that accounts for the longitudinal wake induced in the structure by the beam. These quantities may be written

$$G_0 = \sqrt{\frac{Z_C P}{\lambda^2}}, \qquad G_H = \frac{qcZ_H}{\lambda^2}, \tag{A2}$$

where Z_C is the characteristic impedance and Z_H is the Cherenkov wake impedance. A conservative approximation for the latter, $Z_H \approx \pi Z_0 \lambda^2/(16a^2)$, is provided by Ref. [58] for the case of a flat (2D) geometry with a beam charge q in a narrow channel, where Z_0 is the impedance of

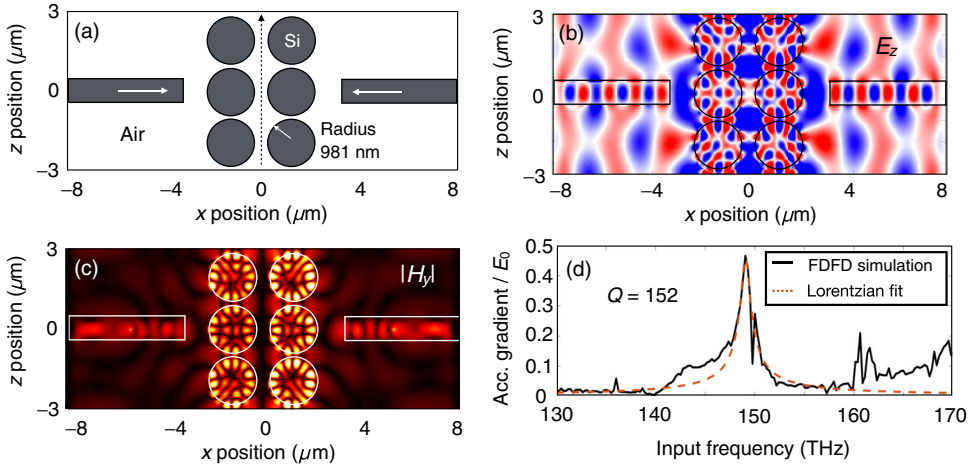

FIG. 8. (a) A schematic of the waveguide to DLA connection. Silicon dual pillars with an optimized radius of 981 nm and a gap size of 400 nm are used. (b) The accelerating electric field during one time step. (c) Absolute value of the transverse magnetic field. (d) Absolute value of the acceleration gradient as a function of frequency, normalized by the peak electric field in the waveguide. A Lorentzian line shape is fit to the square of this plot. The square root of this fit is shown in red. Based on the Lorentzian fit, a Q factor of 152 ± 29 is determined. As computed following the derivation in Ref. [6], but with the waveguide mode impedance and effective area in place of the plane-wave values, this structure has a shunt impedance, Z_S, of 449.1 Ω over three periods and a Z_S/Q value of 2.95 Ω.

free space and we take $a = 200$ nm to be the half-width of the accelerating channel. The resulting efficiency η_q is then quadratic in the charge q. Solving for the maximal value gives optimal bunch charge and efficiency,

$$q_{\text{opt}} = \frac{G_0 \lambda^2}{2cZ_H}, \qquad \eta_{q_{\text{opt}}} = \frac{1}{4}\frac{\Delta z}{c\tau}\frac{Z_C}{Z_H}. \tag{A3}$$

For the present case, with $Z_C = 149\ \Omega$, $Z_H = 7402\ \Omega$, and $G_0 = 108\,\text{MV/m}$, we obtain $q_{\text{opt}} \approx 0.1\,\text{fC}$ and $\eta_{q_{\text{opt}}} \approx 0.04\%$, corresponding to a retarding gradient $G_H = 54$ MV/m and thus a beam-loaded gradient $G = G_0/2$. The optimal charge corresponds to 608 electrons, which is consistent with achieved laser-triggered emission from nanotip electron sources. As shown in Ref. [59], under multibunch operation with structures designed for higher gradients, efficiencies can theoretically be in the tens of percent. The structure design considered here is intended to illustrate the basic principles of constructing a multiguided wave system and is not optimized for efficient beam coupling. Even so, efficiencies of this order are still acceptable for possible near-term applications, such as a 1-MeV to 10-MeV medical linear accelerator, where the requisite beam powers are less than 1 W.

8. Heat dissipation

The laser input pulse energy at each stage of length $L = 192\ \mu$m is $E_p = 11$ nJ for the SiN case in Table II. We assume a repetition rate $f_{\text{rep}} = 10$ MHz, which is consistent with commercially available solid-state fiber lasers at microjoule pulse energies. Given that there are two input laser couplings per stage of length L in the configuration of Fig. 1, the average laser power per unit length of accelerator is $dP/dz \approx 11$ W/cm. Making a conservative assumption that all of this power passes through solid silicon, which has an absorption coefficient of $\alpha_{\text{Si}} = 0.027\ \text{cm}^{-1}$ at $\lambda = 2\ \mu$m, the corresponding absorbed power is on the order of 6 mW/cm^2. This power is more than 5 orders of magnitude lower than the technological limit for heat dissipation from planar surfaces, where 1 kW/cm^2 is typical [60,61]. Prior work has shown that near-critical coupling to silicon dielectric accelerator structures using SOI waveguides is possible with the appropriate phase adjustment to produce a traveling-wave match between the input and output couplers [62]. The last work was for a structure design based on a 3D photonic crystal, but it illustrates the principle that more sophisticated power-handling techniques can potentially be employed in future designs to remove laser power from the wafer and safely dump it away from the accelerator.

APPENDIX B: TREE-NETWORK STRUCTURE—VELOCITY MATCHING TO ELECTRON BEAM

Using the circular bending geometry as described in Fig. 9, we calculate a delay to the pulse to match the electron velocity in the DLA structure. For a given vertical distance h and waveguide group index n_g, we seek to set a condition on R to accomplish this delay. First, we may establish the value of the bend angle θ as

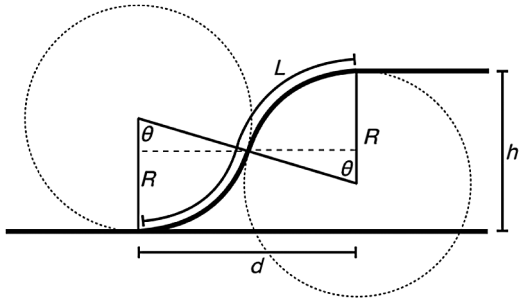

FIG. 9. Diagram of a single bend in the tree-network structure with an optical pulse incident from the left. The bend has radius R and accomplishes a vertical climb of h over a horizontal distance d. The total length of the bent section is L. The electron travels from bottom to top in this configuration. We wish to find an R such that an optical pulse traveling through the bent section is delayed by the same amount of time for the electron to travel the vertical distance h.

$$\theta = \begin{cases} \cos^{-1}(1 - h/2R) & \text{if } h < 2R \\ \pi/2 & \text{if } h \geq 2R \end{cases}. \tag{B1}$$

When $h \geq 2R$, we use two 90° bends and extend the intermittent length with a vertical waveguide section. From this expression, we can express the horizontal distance d as

$$d = 2R\sin(\theta), \tag{B2}$$

and the total length of the bent waveguide as

$$L = \begin{cases} 2R\theta & \text{if } h < 2R \\ h + (\pi - 2)R & \text{if } h \geq 2R \end{cases}. \tag{B3}$$

To now set a condition on R, we insist that the pulse timing delay between the curved waveguide and the straight waveguide is equal to the time needed for the electron to travel a distance h. The difference in length between the curved waveguide and the straight waveguide is simply $L - d$; thus, the timing delay of the pulse is given by

$$\begin{aligned} \Delta t_{\text{pulse}} &= \frac{n_g}{c_0}(L - d) \\ &= \frac{n_g}{c_0}\begin{cases} 2R[\theta - \sin(\theta)] & \text{if } h < 2R \\ h + R(\pi - 4) & \text{if } h \geq 2R \end{cases}. \end{aligned} \tag{B4}$$

The electron has a velocity of βc_0, so its timing delay is given by

$$\Delta t_{e^-} = \frac{h}{\beta c_0}. \tag{B5}$$

Setting these two expressions equal and solving for R, we find that

$$R = \frac{h}{\beta n_g}\begin{cases} 2[\theta - \sin(\theta)]^{-1} & \text{if } h < 2R \\ \frac{\beta n_g - 1}{4-\pi} & \text{if } h \geq 2R \end{cases}. \tag{B6}$$

Thus, for extended interaction lengths where $h \gg 2R$, we require that $\beta n_g > 1$ for a positive (and physical) solution for R. Equivalently, for low β values, we require large n_g values in order to sufficiently delay the pulse in order to match the low electron velocity.

APPENDIX C: WAVEGUIDE NONLINEARITIES

To study waveguide nonlinearity, we solve a version of the nonlinear Schrödinger equation (NLSE), which is typically used for describing nonlinear propagation of a pulse with a duration between 10 fs and 10 ns. In this particular treatment, the solution for the electric field is assumed to be of the form of Eq. (C1), where the slowly varying envelope approximation and separation of variables of the modal distribution $F(x, y)$ and envelope $A(z, t)$ are used [63].

$$\mathbf{E}(\mathbf{r}, t) = \frac{\hat{x}}{2}\{F(x, y)A(z, t)\exp[i(\beta_0 z - \omega_0 t)] + \text{c.c.}\}, \tag{C1}$$

where x and y are the transverse directions, z is the propagation direction, β_0 is the propagation constant, and ω_0 is the optical frequency.

The slowly varying envelop $A(z, t)$ obeys the form of the NLSE given in Eq. (C2), which can be solved by the split-step method [64],

$$\frac{\partial A}{\partial z} + \frac{\alpha}{2}A + \frac{i\beta_2}{2}\frac{\partial^2 A}{\partial T^2} - \frac{\beta_3}{6}\frac{\partial^3 A}{\partial T^3} = i\gamma\left(|A|^2 A + \frac{i}{\omega_0}\frac{\partial}{\partial T}(|A|^2 A) - T_R A\frac{\partial |A|^2}{\partial T}\right), \tag{C2}$$

where $T = t - z/v_g$ is the time in the retarded frame, with v_g being the group velocity, $\gamma = 2\pi n_2/(\lambda A_{\text{eff}})$ is the nonlinear parameter per unit length and power, and A_{eff} is the effective modal area. T_R is the Raman time constant and has an approximated value of 3 fs [65]. On the left-hand side of this equation, the loss is incorporated into the second term, with α being the loss of the waveguide in units of m^{-1}. The third and fourth terms indicate second- and third-order dispersion, with β_2 and β_3 being the respective dispersion coefficients. On the right-hand side of the equation, the first term is SPM, the second term is self-steepening, and the third term is Raman scattering.

For our proposed structure, the overall length of the waveguide is short ($\ll 1$ m); hence, material loss α can be neglected. The dispersion terms come from both the material dispersion and the waveguide dispersion. These terms, $\beta_{2,\text{wg}}$ and $\beta_{3,\text{wg}}$, can be obtained by numerically solving for the effective refractive index as a function of wavelength $n_{\text{eff}}(\lambda)$, and they are explicitly given as

$$\beta_{2,\text{wg}} = \frac{\lambda^3}{2\pi c^2}\frac{d^2 n_{\text{eff}}}{d\lambda^2}, \tag{C3}$$

$$\beta_{3,\text{wg}} = -\frac{3\lambda^4}{4\pi^2 c^3}\frac{d^2 n_{\text{eff}}}{d\lambda^2} - \frac{\lambda^5}{4\pi^2 c}\frac{d^3 n_{\text{eff}}}{d\lambda^3}. \tag{C4}$$

We note that the contribution of dispersion and SPM is generally compared through the N^2 parameter [63]:

$$N^2 = \frac{L_D}{L_{\text{NL}}} = \frac{\gamma P_0 \tau^2}{|\beta_2|}, \tag{C5}$$

where τ is the pulse duration. When the dispersion length, L_D, is larger than the nonlinear length, L_{NL}, SPM is dominant over dispersion and $N^2 > 1$. SPM is typically large in strongly guiding and high n_2 materials, such as the strongly guiding SOI waveguide. For the weakly guiding, lower n_2 SiN waveguides, SPM is less prominent, yet still larger than dispersive effects for the range of peak powers we consider. Using typical experimental parameters and examining the material considered in this paper with the lowest nonlinearity (SiO_2), we have $n_2(SiO_2) = 2.6\ \text{m}^2/\text{W}$, $A_{\text{eff}} \sim 7\ \mu\text{m}^2$, $|\beta_2| = 76\ \text{fs}^2/\text{mm}$, and a peak power of $P_0 = 80$ kW, with the corresponding $N^2 = 758$, indicating that SPM is highly dominant over dispersion.

Alternatively, by turning on and off each term in Eq. (C2) to investigate its contribution, we find that, for both the SOI and SiN cases, SPM is indeed the dominant contribution to the nonlinearity; other terms do not yield a significant difference to the results for a propagation distance on the order of hundreds of micrometers. Hence, our choice of SPM as the dominant nonlinearity in the parameter study is justified.

APPENDIX D: DERIVATION OF MINIMUM INPUT FIELD BEFORE DAMAGE OR NONLINEARITIES

In this section, we give expressions for the maximum peak electric fields, denoted by E_0, that we may inject into our waveguide system before each constraint becomes relevant.

1. Input damage

Fields at the input are damaged if they exceed the damage threshold of the coupling material. Thus, we enforce the condition that

$$E_0 < E_d(\tau). \tag{D1}$$

2. Accelerator damage

With a given tree-network structure, we introduce a total of N_s separate $1 \to 2$ power splits for an input pulse. Furthermore, we introduce some optical-power loss characterized by the power efficiencies of the input coupler (η_c), splitters (η_s), and bends (η_s). Thus, the field at the output port of the laser coupling structure, E_{out}, is given by

$$E_{\text{out}} = E_0 \left(2^{-N_s} \eta_c \eta_s^{N_s} \eta_b^{N_s} \right)^{1/2}. \tag{D2}$$

As we show in Appendix E, resonance in the DLA structures with quality factor Q will lead to a field enhancement in the accelerator gap that scales as $\sqrt{Q}$. Since our damage will be caused by the maximum field in the DLA materials, we assume there is another constant factor, f_m, relating the maximum field in the DLA material to the average field in the accelerator gap. From simulations, we estimate the value of f_m to be 2. Thus, the maximum field in the DLA material is

$$\begin{aligned} E_{\text{mat}} &= E_{\text{out}} f_m \sqrt{Q} \\ &= E_0 f_m \sqrt{Q} \left(2^{-N_s} \eta_c \eta_s^{N_s} \eta_b^{N_s} \right)^{1/2}. \end{aligned} \tag{D3}$$

We require the maximum field in the DLA material to be lower than the damage threshold, giving the constraint that

$$E_0 < E_d(\tau) \frac{2^{N_s/2}}{f_m \sqrt{Q}} \left(\eta_c \eta_s^{N_s} \eta_b^{N_s} \right)^{-1/2}. \tag{D4}$$

3. Self-phase modulation

For a wave of power P_0 and wavelength λ traveling a distance L in a material with cross-section area A and nonlinear refractive index n_2, the accumulated SPM phase is given by [66]

$$\Delta\phi_{\text{SPM}} = 2\pi \frac{n_2 P L}{A\lambda}. \tag{D5}$$

Since the optical power in our waveguides is traveling in several materials, each with a different nonlinear refractive index, we define an effective n_2 value for modeling that is given by

$$n_2^{(\text{eff})} = \frac{1}{P^{(\text{tot})}} \sum_{j=1}^{\text{num mat}} n_2^{(j)} P^{(j)}, \tag{D6}$$

where $P^{(\text{tot})}$ is the total optical power carried by the waveguide and $P^{(j)}$ is the amount of power traveling in material j.

Furthermore, the optical power is split in half at each bend, so we must take this fact into account in our SPM calculation. Taking into account the losses in our system, the final expression for the amount of the SPM phase is

$$\Delta\phi_{\text{SPM}} = 2\pi \frac{n_2^{(\text{eff})} P_0 \eta_c}{A_{\text{eff}} \lambda} \sum_{i=0}^{N_s} \frac{\eta_s^i \eta_b^i L_i}{2^i}. \tag{D7}$$

Once the SPM phase reaches a value of 2π, we notice pulse deformation leading to degradation of the acceleration gradient. This approximation is confirmed by full simulations with our NLSE solver, as described in Appendix C. Thus, the constraint on our input field to avoid SPM effects is given by

$$E_0 < \left(\frac{2\lambda}{n_2^{(\text{eff})} n c_0 \epsilon_0 \eta_c} \sum_{i=0}^{N_s} \frac{2^i}{\eta_s^i \eta_b^i L_i} \right)^{1/2}. \tag{D8}$$

APPENDIX E: DLA RESONANCES

In this appendix, we derive the analytical form of the resonant field enhancement in the accelerator gap and verify that it is approximately proportional to $\sqrt{Q}$. The resonant nature of the acceleration structure can by described by coupled-mode theory [67,68]. We denote the amplitude of the resonant mode as s, where $|s|^2$ represents the energy stored in the resonant mode, and the amplitudes of incoming and outgoing waves as $\boldsymbol{a}$ and $\boldsymbol{b}$, respectively, where $\boldsymbol{a}^\dagger \boldsymbol{a}$ and $\boldsymbol{b}^\dagger \boldsymbol{b}$ represent the power of the incoming and outgoing waves. The dynamics of the resonant mode can be described as

$$\frac{ds}{dt} = (-i\omega_0 - \gamma_s) s + \boldsymbol{\kappa}^T \boldsymbol{a}, \tag{E1a}$$

$$\boldsymbol{b} = B\boldsymbol{a} + s\boldsymbol{d}, \tag{E1b}$$

where ω_0 is the resonant frequency of the acceleration mode, γ_s is the leakage rate resulting from the coupling to outgoing waves, and B is the background scattering matrix including direct pathways. $\boldsymbol{\kappa}$ and $\boldsymbol{d}$ are coupling coefficients for the incoming and outgoing waves. In a reciprocal system with lossless materials [68], which is the case for a DLA,

$$\boldsymbol{\kappa} = \boldsymbol{d}, \tag{E2a}$$

$$\boldsymbol{d}^\dagger \boldsymbol{d} = 2\gamma_s. \tag{E2b}$$

The periodic acceleration structure has two channels for incoming and outgoing propagation waves to couple to the resonant mode. As the acceleration mode is an even mode which has a nonvanishing longitudinal electric field at the mirror plane, the incident waves from the left and the right

should have equal amplitude and phase to efficiently excite the acceleration mode. Thus, $\boldsymbol{a} = [1,1]^T a_1$, where $|a_1|^2$ represents the power of the incoming waves from the left channel. The even mode also couples equally to the left and the right channel. As a result, $\boldsymbol{d} = [1,1]^T d_1$, where d_1 is the coupling coefficient for the outgoing waves in the left channel and $|d_1|^2 = \gamma_s$, according to Eq. (E2).

From Eq. (E1), we obtain $s(\omega) = \{[\boldsymbol{\kappa}^T \boldsymbol{a}^+(\omega)]/[-i(\omega-\omega_0)+\gamma_s]\}$ for each frequency component. Based on the preceding analysis, we determine the spectrum of energy stored in the resonant mode as

$$|s(\omega)|^2 = \frac{4\gamma|a_1^+(\omega)|^2}{(\omega-\omega_0)^2+\gamma_s^2}. \tag{E3}$$

To give an explicit expression about the field enhancement, we denote the maximum electric-field amplitude at the output port of the power delivery waveguide as E_{out} and the maximum amplitude of the electric field inside the acceleration structure as E_{mat}. We introduce the effective incident spot area (S) such that the incident power from, say, the left channel is $[1/(2\eta_0)]|E_{\text{out}}|^2 S$, and define the mode volume (V) of the resonant mode so that the energy stored in the resonant mode is $\frac{1}{2}\epsilon_r\epsilon_0|E_{\text{mat}}|^2 V$ [69], where ϵ_r is the relative permittivity of the dielectric accelerator. Thus,

$$|E_{\text{mat}}(\omega)| = \left(\frac{8cS}{\epsilon_r\omega_0 V}\right)^{1/2}\left[\frac{\gamma_s^2}{(\omega-\omega_0)^2+\gamma_s^2}\right]^{1/2}\sqrt{Q}|E_{\text{out}}(\omega)|, \tag{E4}$$

where the quality factor Q is inversely proportional to the resonant-mode leakage rate, i.e., $Q = [\omega_0/(2\gamma_s)]$. Equation (E4) shows that the field enhancement in the resonant accelerator structure is proportional to $\sqrt{Q}$ and has a bandwidth that decreases with an increasing Q value, where the frequency dependence is the square root of a Lorentzian line shape.

APPENDIX F: CALCULATION OF THE ACCELERATION GRADIENT

Here, we formalize the calculation of the acceleration gradient used in the parameter study. In the two following subsections, we show how to deal with both arbitrary, finite-duration input pulses and finite-stage-length structures. In both derivations, we assume an input pulse $E_0(t)$, which leads to the creation of an accelerating field in the gap of a unit cell $E_z(z,t)$ through the convolution with the corresponding impulse response function $f(z,t)$. In the frequency domain, this operation is done via multiplication of the pulse spectrum $E_0(\omega)$ by the transfer function $F(z,\omega)$:

$$E_z(z,t) = E_0(t) \circ f(z,t), \tag{F1}$$

$$E_z(z,\omega) = E_0(\omega)F(z,\omega). \tag{F2}$$

1. Finite pulse duration

We wish to derive the correspondence between the time-domain description of the acceleration gradient, given an arbitrary input pulse, and the frequency-domain approach that is used in this work and others [6,39].

In the time domain, the acceleration gradient is expressed as an integral over the accelerating electric field over the particle's trajectory:

$$G = \frac{1}{L}\int_{-L/2}^{L/2} dz\, E_z[z,t(z)]. \tag{F3}$$

If the electron moves uniformly in $\hat{z}$ with speed βc_0, then $z(t) = z_0 + \beta c_0 t$ and we may express the acceleration gradient as a function of the starting time, t_0, as

$$\begin{aligned} G(t_0) &= \frac{1}{L}\int_{-L/2}^{L/2} dz E_z(z, t_0 + z/\beta c_0) \\ &= \frac{1}{L}\int_{-L/2}^{L/2} dz \int_{-\infty}^{\infty} dt E_z(z,t)\delta(t - t_0 - z/\beta c_0). \end{aligned} \tag{F4}$$

In previous works, such as Ref. [6], the acceleration gradient is computed by first performing a finite-difference time-domain simulation to record $E_z(z,t)$ along the gap for a series of time, then maximizing the integral in Eq. (F4) with respect to t_0. However, we may, equivalently, do the computation in the frequency domain by Fourier transforming this equation with respect to t_0, which yields

$$\begin{aligned} G(\omega) &= \frac{1}{L}\int_{-L/2}^{L/2} dz \int_{-\infty}^{\infty} dt E_z(z,t) e^{i\omega(t - z/\beta c_0)} \\ &= \frac{1}{L}\int_{-L/2}^{L/2} dx e^{-i\omega z/\beta c_0} \int_{-\infty}^{\infty} dt E_z(z,t) e^{i\omega t} \\ &= \frac{1}{L}\int_{-L/2}^{L/2} dz e^{-i\omega z/\beta c_0} E_0(\omega) F(z,\omega) \\ &\equiv g(\omega) E_0(\omega). \end{aligned} \tag{F5}$$

Here, $g(\omega)$ is the gradient normalized by the incident electric field at that frequency, $E_0(\omega)$, which is also described in the following subsection. Now, by performing a series of FDFD simulations at discrete frequencies, we may estimate $F(z,\omega)$. Then, using the known pulse amplitude spectrum and phase information in $E_0(\omega)$, we can compute $G(\omega)$ as described. Finally, $G(t_0)$ can be determined by applying an inverse discrete Fourier transform on $G(\omega)$, and the acceleration gradient can then be found by taking the maximum of the absolute value of this quantity. Explicitly,

$$G = \max_{t_0} |\mathcal{F}^{-1}\{g(\omega)E_0(\omega)\}|. \tag{F6}$$

2. Finite stage length

Now, let us assume that we have a DLA with a stage length of L along $\hat{z}$ with an incident laser pulse of the form $E_0(t)$ with spectrum $E_0(\omega)$. The laser is assumed to be spatially uniform along the entire interaction length. We use the same transfer-function formalism as was introduced at the beginning of this section.

The DLA structure is further assumed to be periodic in $\hat{z}$ with a periodicity of $\Lambda_z = \beta\lambda = 2\pi c_0/\omega_0$. Thus, the fields can be expressed as a Fourier series,

$$E_z(z,\omega) = E_0(\omega)\sum_{m=-\infty}^{\infty} T_m(\omega)e^{imz\omega_0/\beta c_0}, \tag{F7}$$

where the $T_m(\omega)$ terms are the spatial Fourier amplitudes of the transfer function $F(z,\omega)$. See Ref. [70] for a similar discussion.

The acceleration gradient at frequency ω, $G(\omega)$, can be written as the average E_z felt by the particle as it moves with velocity $\beta c_0\hat{z}$ through the entire interaction length of the structure from $z = -L/2$ to $z = L/2$:

$$\begin{aligned} G(\omega) &= \frac{1}{L}\int_{-L/2}^{L/2} dz E_z(z,\omega)e^{iz\omega/\beta c_0} \\ &= \frac{1}{L}\int_{-L/2}^{L/2} dz E_0(\omega)\sum_{m=-\infty}^{\infty} T_m(\omega)e^{i(m\omega_0+\omega)z/\beta c_0}. \end{aligned} \tag{F8}$$

Rearranging the integral and defining the normalized gradient $g(\omega) \equiv G(\omega)/E_0(\omega)$,

$$\begin{aligned} g(\omega) &= \frac{1}{L}\sum_{m=-\infty}^{\infty} T_m(\omega)\int_{-L/2}^{L/2} dz e^{i(m\omega_0+\omega)z/\beta c_0} \\ &= \sum_{m=-\infty}^{\infty} T_m(\omega)\frac{2\beta c_0 \sin\left(\frac{L}{2\beta c_0}(m\omega_0+\omega)\right)}{L(m\omega_0+\omega)} \\ &= \sum_{m=-\infty}^{\infty} T_m(\omega)\mathrm{sinc}\left(\frac{L}{2\beta c_0}(m\omega_0+\omega)\right). \end{aligned} \tag{F9}$$

We reasonably assume that the input pulse power is centered around ω_0. In this case, then, only the $m = -1$ value will contribute to the accelerating mode. We could also choose a higher order, $m = -2, -3, \ldots$, for the accelerating mode, as was demonstrated previously [5,71], but $m = -1$ is chosen for simplicity. Thus, as the interaction length increases, the $\mathrm{sinc}(\cdots)$ function becomes more tightly centered around $\omega = \omega_0$, limiting the available bandwidth of the input pulse.

Under this assumption, the final form of the normalized gradient becomes

$$g(\omega) = T_{-1}(\omega)\mathrm{sinc}\left(\frac{L}{2\beta c_0}(\omega-\omega_0)\right). \tag{F10}$$

Assuming that $T_{-1}(\omega)$ is relatively constant over a bandwidth larger than our input pulse, we see that the gradient falls to zero at $\omega = \omega_0 \pm [(2\pi\beta c_0)/L]$. For a Gaussian pulse of duration τ with a time-bandwidth product of 0.44, the gradient falls to zero at

$$L = \tau\frac{4\pi\beta c_0}{0.44}. \tag{F11}$$

For a τ value of 250 fs and a β value of 1, this expression corresponds to a stage length of 2.14 mm. Thus, to satisfy the bandwidth requirement, L must be much less than 2.14 mm if no pulse-delay techniques are used.

This result can be compared to the following back-of-the-envelope calculation: An electron traveling over a length L with speed βc_0 will spend $\Delta t_{e^-} = [L/(\beta c_0)]$ of time in the channel. The input pulse will spend approximately τ seconds in the gap. Thus, for the fields to be present during the whole duration,

$$L < \tau\beta c_0. \tag{F12}$$

This length scales with τ, β, and c_0 in the same fashion as Eq. (F11), which serves as a sanity check. However, the full expression in Eq. (F10) can be used to rigorously compute the effect that a finite-stage-length structure will have on the acceleration gradient.

[1] E. A. Peralta, K. Soong, R. J. England, E. R. Colby, Z. Wu, B. Montazeri, C. McGuinness, J. McNeur, K. J. Leedle, D. Walz, E. B. Sozer, B. Cowan, B. Schwartz, G. Travish, and R. L. Byer, Demonstration of electron acceleration in a laser-driven dielectric microstructure, Nature (London) **503**, 91 (2013).

[2] Kent P. Wootton, Ziran Wu, Benjamin M. Cowan, Adi Hanuka, Igor V. Makasyuk, Edgar A. Peralta, Ken Soong, Robert L. Byer, and R. Joel England, Demonstration of acceleration of relativistic electrons at a dielectric microstructure using femtosecond laser pulses, Opt. Lett. **41**, 2696 (2016).

[3] Kenneth J. Leedle, Andrew Ceballos, Huiyang Deng, Olav Solgaard, R. Fabian Pease, Robert L. Byer, and James S. Harris, Dielectric laser acceleration of sub-100 keV electrons with silicon dual-pillar grating structures, Opt. Lett. **40**, 4344 (2015).

[4] Kenneth J. Leedle, R. Fabian Pease, Robert L. Byer, and James S. Harris, Laser acceleration and deflection of 96.3 keV electrons with a silicon dielectric structure, Optica **2**, 158 (2015).

[5] John Breuer and Peter Hommelhoff, Laser-Based Acceleration of Nonrelativistic Electrons at a Dielectric Structure, Phys. Rev. Lett. **111**, 134803 (2013).

[6] T. Plettner, P. P. Lu, and R. L. Byer, Proposed few-optical cycle laser-driven particle accelerator structure, Phys. Rev. ST Accel. Beams **9**, 111301 (2006).
[7] D. Cesar, S. Custodio, J. Maxson, P. Musumeci, X. Shen, E. Threlkeld, R. J. England, A. Hanuka, I. V. Makasyuk, E. A. Peralta, K. P. Wootton, and Z. Wu, Onset of nonlinear effects in a high gradient dielectric laser accelerator, arXiv:1707.02364.
[8] M. Kozák, M. Förster, J. McNeur, N. Schönenberger, K. Leedle, H. Deng, J. S. Harris, R. L. Byer, and P. Hommelhoff, Dielectric laser acceleration of sub-relativistic electrons by few-cycle laser pulses, Nucl. Instrum. Methods Phys. Res., Sect. A **865**, 84 (2017).
[9] M. Kozák, P. Beck, H. Deng, J. McNeur, N. Schönenberger, C. Gaida, F. Stutzki, M. Gebhardt, J. Limpert, A. Ruehl *et al.*, Acceleration of sub-relativistic electrons with an evanescent optical wave at a planar interface, Opt. Express **25**, 19195 (2017).
[10] N. A. Solyak, Gradient limitations in room temperature and superconducting acceleration structures, AIP Conf. Proc. **1086**, 365 (2009).
[11] Motoichi Ohtsu and Hirokazu Hori, *Near-Field Nano-optics: From Basic Principles to Nano-fabrication and Nano-photonics* (Springer Science+Business Media, New York, 2012).
[12] Evgenya I. Simakov, Heather L. Andrews, Matthew J. Herman, Kevin M. Hubbard, and Eric Weis, Diamond field emitter array cathodes and possibilities of employing additive manufacturing for dielectric laser accelerating structures, AIP Conf. Proc. **1812**, 060010 (2017).
[13] Yasuhiko Arakawa, Takahiro Nakamura, Yutaka Urino, and Tomoyuki Fujita, Silicon photonics for next generation system integration platform, IEEE Commun. Mag. **51**, 72 (2013).
[14] Andy Eu-Jin Lim, Junfeng Song, Qing Fang, Chao Li, Xiaoguang Tu, Ning Duan, Kok Kiong Chen, Roger Poh-Cher Tern, and Tsung-Yang Liow, Review of silicon photonics foundry efforts, IEEE J. Sel. Top. Quantum Electron. **20**, 405 (2014).
[15] David Thomson, Aaron Zilkie, John E. Bowers, Tin Komljenovic, Graham T. Reed, Laurent Vivien, Delphine Marris-Morini, Eric Cassan, Léopold Virot, Jean-Marc Fédéli, Jean-Michel Hartmann, Jens H. Schmid, Dan-Xia Xu, Frédéric Boeuf, Peter O'Brien, Goran Z. Mashanovich, and M. Nedeljkovic, Roadmap on silicon photonics, J. Opt. **18**, 073003 (2016).
[16] B. C. Stuart, M. D. Feit, A. M. Rubenchik, B. W. Shore, and M. D. Perry, Laser-Induced Damage in Dielectrics with Nanosecond to Subpicosecond Pulses, Phys. Rev. Lett. **74**, 2248 (1995).
[17] An-Chun Tien, Sterling Backus, Henry Kapteyn, Margaret Murnane, and Gérard Mourou, Short-Pulse Laser Damage in Transparent Materials as a Function of Pulse Duration, Phys. Rev. Lett. **82**, 3883 (1999).
[18] Yong Jee, Michael F. Becker, and Rodger M. Walser, Laser-induced damage on single-crystal metal surfaces, J. Opt. Soc. Am. B **5**, 648 (1988).
[19] Kazuyoshi Koyama, Shohei Otsuki, Mitsuru Uesaka, Mitsuhiro Yoshida, and Aimiding Aimidula, Parameter study of a laser-driven dielectric accelerator for radiobiology research, J. Phys. B **47**, 234005 (2014).
[20] R. Joel England *et al.*, Dielectric laser accelerators, Rev. Mod. Phys. **86**, 1337 (2014).
[21] K. P. Wootton, J. McNeur, and K. J. Leedle, Dielectric laser accelerators: Designs, experiments, and applications, Rev. Accel. Sci. Techol. **09**, 105 (2016).
[22] Uwe Niedermayer, Thilo Egenolf, and Oliver Boine-Frankenheim, Beam dynamics analysis of dielectric laser acceleration using a fast 6D tracking scheme, Phys. Rev. Accel. Beams **20**, 111302 (2017).
[23] B. Naranjo, A. Valloni, S. Putterman, and J. B. Rosenzweig, Stable Charged-Particle Acceleration and Focusing in a Laser Accelerator Using Spatial Harmonics, Phys. Rev. Lett. **109**, 164803 (2012).
[24] K. P. Wootton, D. B. Cesar, B. M. Cowan, A. Hanuka, I. V. Makasyuk, J. Maxson, E. A. Peralta, K. Soong, Z. Wu, R. L. Byer, P. Musumeci, and R. J. England, Recent demonstration of record high gradients in dielectric laser accelerating structures, AIP Conf. Proc. **1812**, 060006 (2017).
[25] J. Hebling, Derivation of the pulse front tilt caused by angular dispersion, Opt. Quantum Electron. **28**, 1759 (1996).
[26] Selcuk Akturk, Xun Gu, Erik Zeek, and Rick Trebino, Pulse-front tilt caused by spatial and temporal chirp, Opt. Express **12**, 4399 (2004).
[27] D. Cesar, J. Maxson, P. Musumeci, X. Shen, R. J. England, and K. P. Wootton, Optical design for increased interaction length in a high gradient dielectric laser accelerator, arXiv:1801.01115.
[28] Ken Leedle (private communication).
[29] Joshua McNeur, Martin Kozák, Norbert Schönenberger, Kenneth J. Leedle, Huiyang Deng, Andrew Ceballos, Heinar Hoogland, Axel Ruehl, Ingmar Hartl, Ronald Holzwarth *et al.*, Multi-stage acceleration and focusing of free-electron beams with photonic microstructures, arXiv:1604.07684.
[30] See Supplemental Material at http://link.aps.org/supplemental/10.1103/PhysRevApplied.9.054017 for a video showing how this design adds an appropriate delay to the optical pulse to match the moving electron bunch.
[31] B. C. Stuart, M. D. Feit, S. Herman, A. M. Rubenchik, B. W. Shore, and M. D. Perry, Nanosecond-to-femtosecond laser-induced breakdown in dielectrics, Phys. Rev. B **53**, 1749 (1996).
[32] Ken Soong, R. L. Byer, E. R. Colby, R. J. England, and E. A. Peralta, Laser damage threshold measurements of optical materials for direct laser accelerators, in *Proceedings of the 15th Advanced Accelerator Concepts Workshop, Austin, 2012*, edited by R. Zgadzaj, E. Gaul, and M. C. Downer, AIP Conference Proceedings No. 1507 (AIP, New York, 2012), p. 511.
[33] Koji Yamada, Silicon photonic wire waveguides: Fundamentals and applications, in *Silicon Photonics II* (Springer, New York, 2011), p. 1.
[34] T. W. Hughes, DLA laser coupling simulation software, https://github.com/twhughes/DLA-Laser-Coupling-Simulation-Software, 2017.
[35] Wonseok Shin and Shanhui Fan, Choice of the perfectly matched layer boundary condition for frequency-domain

Maxwell's equations solvers, J. Comput. Phys. **231**, 3406 (2012).

[36] Huiyang Deng, Jiaqi Jiang, Yu Miao, Kenneth J. Leedle, Hongquan Li, Olav Solgaard, Robert L. Byer, and James S. Harris, Design of racetrack ring resonator based dielectric laser accelerators, arXiv:1701.08945.

[37] T. Shoji, T. Tsuchizawa, T. Watanabe, K. Yamada, and H. Morita, Low loss mode size converter from 0.3 μm square Si wire waveguides to single-mode fibres, Electron. Lett. **38**, 1669 (2002).

[38] Wesley D. Sacher, Jared C. Mikkelsen, Patrick Dumais, Jia Jiang, Dominic Goodwill, Xianshu Luo, Ying Huang, Yisu Yang, Antoine Bois, Patrick Guo-Qiang Lo *et al.*, Tri-layer silicon nitride-on-silicon photonic platform for ultra-low-loss crossings and interlayer transitions, Opt. Express **25**, 30862 (2017).

[39] Tyler Hughes, Georgios Veronis, Kent P. Wootton, R. Joel England, and Shanhui Fan, Method for computationally efficient design of dielectric laser accelerator structures, Opt. Express **25**, 15414 (2017).

[40] Amit Mizrahi and Levi Schächter, Optical Bragg accelerators, Phys. Rev. E **70**, 016505 (2004).

[41] Uwe Niedermayer, Oliver Boine-Frankenheim, and Thilo Egenolf, Designing a dielectric laser accelerator on a chip, J. Phys.: Conf. Ser. **874**, 012041 (2017).

[42] Y. Wei, G. Xia, J. D. A. Smith, and C. P. Welsch, Dual-gratings with a Bragg reflector for dielectric laser-driven accelerators, Phys. Plasmas **24**, 073115 (2017).

[43] Michael Belt, Michael L. Davenport, John E. Bowers, and Daniel J. Blumenthal, Ultra-low-loss Ta_2O_5-core/SiO_2-clad planar waveguides on Si substrates, Optica **4**, 532 (2017).

[44] Minhao Pu, Liu Liu, Haiyan Ou, Kresten Yvind, and Jørn M Hvam, Ultra-low-loss inverted taper coupler for silicon-on-insulator ridge waveguide, Opt. Commun. **283**, 3678 (2010).

[45] Dirk Taillaert, Frederik Van Laere, Melanie Ayre, Wim Bogaerts, Dries Van Thourhout, Peter Bienstman, and Roel Baets, Grating couplers for coupling between optical fibers and nanophotonic waveguides, Jpn. J. Appl. Phys. **45**, 6071 (2006).

[46] Yunhong Ding, Haiyan Ou, and Christophe Peucheret, Ultrahigh-efficiency apodized grating coupler using fully etched photonic crystals, Opt. Lett. **38**, 2732 (2013).

[47] Arman B. Fallahkhair, Kai S. Li, and Thomas E. Murphy, Vector finite difference modesolver for anisotropic dielectric waveguides, J. Lightwave Technol. **26**, 1423 (2008).

[48] Ami Yaacobi, Jie Sun, Michele Moresco, Gerald Leake, Douglas Coolbaugh, and Michael R. Watts, Integrated phased array for wide-angle beam steering, Opt. Lett. **39**, 4575 (2014).

[49] David Kwong, Amir Hosseini, Yang Zhang, and Ray T. Chen, 1×12 unequally spaced waveguide array for actively tuned optical phased array on a silicon nanomembrane, Appl. Phys. Lett. **99**, 051104 (2011).

[50] Yi Zhang, Shuyu Yang, Andy Eu-Jin Lim, Guo-Qiang Lo, Christophe Galland, Tom Baehr-Jones, and Michael Hochberg, A compact and low loss Y-junction for submicron silicon waveguide, Opt. Express **21**, 1310 (2013).

[51] Russell Eberhart and James Kennedy, A new optimizer using particle swarm theory, in *Proceedings of the Sixth International Symposium on Micro Machine and Human Science (MHS '95), Nagoya, Japan, 1995* (IEEE, New York, 1995), p. 39.

[52] Christopher M. Lalau-Keraly, Samarth Bhargava, Owen D. Miller, and Eli Yablonovitch, Adjoint shape optimization applied to electromagnetic design, Opt. Express **21**, 21693 (2013).

[53] Alexander Y. Piggott, Jan Petykiewicz, Logan Su, and Jelena Vučković, Fabrication-constrained nanophotonic inverse design, Sci. Rep. **7**, 1786 (2017).

[54] Elena I. Smotrova, Alexander I. Nosich, Trevor M. Benson, and Phillip Sewell, Cold-cavity thresholds of microdisks with uniform and nonuniform gain: Quasi-3-D modeling with accurate 2-D analysis, IEEE J. Sel. Top. Quantum Electron. **11**, 1135 (2005).

[55] David Kwong, Amir Hosseini, John Covey, Yang Zhang, Xiaochuan Xu, Harish Subbaraman, and Ray T Chen, On-chip silicon optical phased array for two-dimensional beam steering, Opt. Lett. **39**, 941 (2014).

[56] Menno Poot and Hong X. Tang, Broadband nanoelectromechanical phase shifting of light on a chip, Appl. Phys. Lett. **104**, 061101 (2014).

[57] R. H. Siemann, Energy efficiency of laser driven, structure based accelerators, Phys. Rev. ST Accel. Beams **7**, 061303 (2004).

[58] K. Bane and G. Stupakov, Using surface impedance for calculating wakefields in flat geometry, Phys. Rev. ST Accel. Beams **18**, 034401 (2015).

[59] Y. C. Niel Na, R. H. Siemann, and R. L. Byer, Energy efficiency of an intracavity coupled, laser-driven linear accelerator pumped by an external laser, Phys. Rev. ST Accel. Beams **8**, 031301 (2005).

[60] J. M. Eggleston, T. J. Kan, K. Kuhn, J. Unternahrer, and R. L. Byer, The slab geometry laser—Part I: Theory, IEEE J. Quantum Electron. **20**, 289 (1984).

[61] T. S. Rutherford, W. M. Tulloch, E. K. Gustafson, and R. L. Byer, Edge-pumped quasi-three-level slab lasers: Design and power scaling, IEEE J. Quantum Electron. **36**, 205 (2000).

[62] Z. Wu, R. J. England, C.-K. Ng, B. Cowan, C. McGuinness, C. Lee, M. Qi, and S. Tantawi, Coupling power into accelerating mode of a three-dimensional silicon woodpile photonics band-gap waveguide, Phys. Rev. ST Accel. Beams **17**, 081301 (2014).

[63] Govind P. Agrawal, *Nonlinear Fiber Optics* (Academic Press, New York, 2007).

[64] J. A. C. Weideman and B. M. Herbst, Split-step methods for the solution of the nonlinear Schrödinger equation, SIAM J. Numer. Anal. **23**, 485 (1986).

[65] A. K. Atieh, P. Myslinski, J. Chrostowski, and P. Galko, Measuring the Raman time constant (T_R) for soliton pulses in standard single-mode fiber, J. Lightwave Technol. **17**, 216 (1999).

[66] Malvin Carl Teich and B. Saleh, *Fundamentals of Photonics*, Wiley Series in Pure and Applied Optics Vol. 3 (Wiley InterScience, Toronto, 1991).

[67] Hermann A. Haus, *Waves and Fields in Optoelectronics* (Prentice-Hall, Englewood Cliffs, NJ, 1984).

[68] Wonjoo Suh, Zheng Wang, and Shanhui Fan, Temporal coupled-mode theory and the presence of non-orthogonal modes in lossless multimode cavities, IEEE J. Quantum Electron. **40**, 1511 (2004).

[69] John David Jackson, *Classical Electrodynamics* (John Wiley & Sons, New York, 2007).

[70] T. Plettner, R. L. Byer, C. McGuinness, and P. Hommelhoff, Photonic-based laser driven electron beam deflection and focusing structures, Phys. Rev. ST Accel. Beams **12**, 101302 (2009).

[71] Josh McNeur, Martin Kozak, Norbert Schönenberger, Ang Li, Alexander Tafel, and Peter Hommelhoff, Laser-driven acceleration of subrelativistic electrons near a nanostructured dielectric grating: From acceleration via higher spatial harmonics to necessary elements of a dielectric accelerator, Nucl. Instrum. Methods Phys. Res., Sect. A **829**, 50 (2016).